Tropopause Evolution in a Rapidly Intensifying Tropical Cyclone: A Static Stability Budget Analysis in an Idealized, Axisymmetric Framework

Patrick Duran* and John Molinari

University at Albany, State University of New York, Albany, NY

**Corresponding author address:* Department of Atmospheric and Environmental Sciences, University at Albany, State University of New York, 1400 Washington Avenue, Albany, NY.

E-mail: pduran2008@gmail.com

ABSTRACT

Large changes in tropopause-layer static stability are observed during the rapid intensification (RI) of an idealized, axisymmetric tropical cyclone (TC). Over the eye, static stability near the tropopause decreases and the cold-point tropopause height rises by up to 4 km at the storm center. Outside of the eye, static stability increases considerably just above the cold-point tropopause, and the tropopause remains near its initial level.

A budget analysis reveals that advection contributes to the static stability tendencies at all times throughout the upper troposphere and lower stratosphere. Advection is particularly important within the eye, where it acts to destabilize the layer near and above the cold-point tropopause. Outside of the eye, a radial-vertical circulation develops during RI, with strong outflow below the tropopause and weak inflow above. Vertical wind shear above and below the upper-tropospheric outflow maximum induces turbulence, which provides forcing for both destabilization and stabilization in the tropopause layer. Meanwhile, as organized convection reaches the tropopause, radiative heating tendencies at the top of the cirrus canopy generally act to destabilize the upper troposphere and stabilize the lower stratosphere. Turbulent mixing and radiative heating combine to play an important role in the development of the strong stable layer immediately above the cold-point tropopause during RI. The results suggest that turbulence and radiation, alongside advection, play fundamental roles in the upper-level static stability evolution of TCs.

1. Introduction

After undergoing a remarkably rapid intensification (RI), Hurricane Patricia (2015) set a new record as the strongest tropical cyclone (TC) ever observed in the Western Hemisphere (Kimberlain et al. 2016; Rogers et al. 2017). High-altitude dropsonde observations taken during the Tropical Cyclone Intensity (TCI) experiment captured this RI in unprecedented detail (Doyle et al. 2017). These observations revealed dramatic changes in the structure of the cold-point tropopause and upper-level static stability as the storm intensified (Duran and Molinari 2018).

At tropical storm intensity, shortly before RI commenced, a strong inversion layer existed just above Patricia's cold-point tropopause, which was located near 17.2 km. During the first half of the RI period, this inversion layer weakened throughout Patricia's inner core, with the weakening most pronounced over the developing eye. By the time the storm reached its maximum intensity, the inversion layer over the eye had disappeared almost completely, which was accompanied by an increase in the tropopause height to a level at or above the highest-available dropsonde data point (18.3 km) at two locations. Meanwhile over the eyewall region, the static stability re-strengthened and the tropopause was limited to a level at or below 17.5 km. The mechanisms that led to these changes in upper-level static stability and tropopause height are the subject of the current paper.

Despite the importance of tropopause-layer thermodynamics in theoretical models of hurricanes (Emanuel and Rotunno 2011; Emanuel 2012), few papers have examined the upper-tropospheric evolution of TCs. Komaromi and Doyle (2017) found that stronger TCs tended to have a higher and warmer tropopause over their inner core than weaker TCs. Their results are consistent with the evolution observed over the inner core of Hurricane Patricia, in which the tropopause height increased and the tropopause temperature warmed throughout RI (Duran and Molinari 2018).

Idealized simulations of a TC analyzed by Ohno and Satoh (2015) suggested that the development of an upper-level warm core near the TC storm center acted to decrease the static stability near the tropopause (compare their Figs. 9,10). Although the mechanisms that drive this static stability evolution have not been examined explicitly, Stern and Zhang (2013) described the development of the TC warm core using a potential temperature (θ) budget analysis. They found that radial and vertical advection both played important roles in warm core development throughout RI, and subgrid-scale diffusion became particularly important during the later stage of RI. To our knowledge, the only paper that has examined explicitly the static stability evolution in a modeled TC is Kepert et al. (2016), but their analysis was limited to the boundary layer. The analysis herein is based upon that of Stern and Zhang (2013), except using a static stability budget similar to that of Kepert et al. (2016), with a focus on the upper troposphere and lower stratosphere.

2. Model Setup

The numerical simulations were performed using version 19.4 of Cloud Model 1 (CM1) described in Bryan and Rotunno (2009). The equations of motion were integrated on a 3000-km-wide, 30-km-deep axisymmetric grid with 1-km horizontal and 250-m vertical grid spacing. The computations were performed on an f-plane at 15°N latitude, over a sea surface with constant temperature of 30.5°C, which matches that observed near Hurricane Patricia (2015; Kimberlain et al. 2016). Horizontal turbulence was parameterized using the Smagorinsky scheme described in Bryan and Rotunno (2009, pg. 1773), with a prescribed mixing length that varied linearly from 100 m at a surface pressure of 1015 hPa to 1000 m at a surface pressure of 900 hPa. This formulation allows for realistically-large horizontal mixing lengths near the hurricane's inner core, consistent with the results of Bryan (2012), while not over-representing horizontal turbulence in convection at outer radii. Vertical turbulence was parameterized using the formulation of Markowski and

Bryan (2016, their Eq. 6), using an asymptotic vertical mixing length of 100 m and a vertically implicit Crank-Nicholson scheme. A Rayleigh damping layer was applied outside of the 2900-km radius and above the 25-km level to prevent spurious gravity wave reflection at the model boundaries. Microphysical processes were parameterized using the Thompson et al. (2004) microphysics scheme and radiative heating tendencies were computed every two minutes using the Rapid Radiative Transfer Model for GCMs (RRTMG) longwave and shortwave schemes (Iacono et al. 2008). The initial temperature and humidity field was horizontally homogeneous and determined by averaging all Climate Forecast System Reanalysis (CFSR) grid points within 100 km of Patricia's center of circulation at 18 UTC 21 October 2015. The vortex described in Rotunno and Emanuel (1987, their Eq. 37) was used to initialize the wind field, setting all parameters equal to the values used therein.

Although hurricanes simulated in an axisymmetric framework tend to be more intense than those observed in nature, the intensity evolution of this simulation matches reasonably well with that observed in Hurricane Patricia. After an initial spin-up period of about 20 hours, the modeled storm (Fig.A1, blue lines) began an RI period that lasted approximately 30 hours. After this RI, the storm continued to intensify more slowly until the maximum 10-m wind speed reached 89 m s^{-1} and the minimum sea-level pressure reached its minimum of 846 mb, 81 hours into the simulation. Hurricane Patricia (red stars) exhibited a similar intensity evolution, with an RI period leading to a maximum 10-m wind speed of 95 m s^{-1} and a minimum sea-level pressure of 872 hPa. Despite the limitations of the axisymmetric framework, the extraordinary intensity of Hurricane Patricia and the rapidity of its intensification makes Patricia a particularly good candidate for axisymmetric analysis.

3. Budget Computation

The static stability can be expressed as the squared Brunt Väisälä frequency:

$$N_m^2 = \frac{g}{T}\left(\frac{\partial T}{\partial z} + \Gamma_m\right)\left(1 + \frac{T}{R_d/R_v + q_s}\frac{\partial q_s}{\partial T}\right) - \frac{g}{1+q_t}\frac{\partial q_t}{\partial z}, \tag{1}$$

where g is gravitational acceleration, T is temperature, R_d and R_v are the gas constants of dry air and water vapor, respectively, q_s is the saturation mixing ratio, q_t is the total condensate mixing ratio, and Γ_m is the moist-adiabatic lapse rate:

$$\Gamma_m = g(1+q_t)\left(\frac{1 + L_v q_s/R_d T}{c_{pm} + L_v \partial q_s/\partial T}\right), \tag{2}$$

where L_v is the latent heat of vaporization and c_{pm} is the specific heat of moist air at constant pressure. In the tropopause layer, q_s, $\partial q_s/\partial T$, and $\partial q_t/\partial z$ approach zero. In this limiting case, Eq. 1 reduces to:

$$N^2 = \frac{g}{\theta}\frac{\partial \theta}{\partial z}, \tag{3}$$

where θ is the potential temperature.

To compute N^2, CM1 uses Eq.1 in saturated environments and Eq. 3 in sub-saturated environments. For simplicity, however, only Eq. 3 will be employed for the budget computations [1].

Taking the time derivative of Eq. 3 yields the static stability tendency:

$$\frac{\partial N^2}{\partial t} = \frac{g}{\theta}\frac{\partial}{\partial z}\frac{\partial \theta}{\partial t} - \frac{g}{\theta^2}\frac{\partial \theta}{\partial z}\frac{\partial \theta}{\partial t}, \tag{4}$$

where the potential temperature tendency, $\partial\theta/\partial t$, can be written:

$$\frac{\partial \theta}{\partial t} = HADV + VADV + HTURB + VTURB + MP + RAD + DISS \tag{5}$$

Each term on the right-hand side of Eq. 5 represents a θ budget variable, each of which is output directly by the model every minute. HADV and VADV are the radial and vertical advective

[1] The validity of this approximation will be substantiated later in this section.

tendencies[2], HTURB and VTURB are the tendencies from the horizontal and vertical turbulence parameterizations, MP is the tendency from the microphysics scheme, RAD is the tendency from the radiation scheme, and DISS is the tendency due to turbulent dissipation. This equation neglects Rayleigh damping, since this term is zero everywhere below 25 km, and the analysis domain does not extend to that level. Each term in Eq. 5 is substituted for $\partial\theta/\partial t$ in Eq. 4, yielding the contribution of each budget term to the static stability tendency. These terms are summed, yielding an instantaneous "budget change" in N^2 every minute. The budget changes are then averaged over 24-hour periods and compared to the total model change in N^2 over that same time period, i.e.:

$$\Delta N^2_{budget} = \frac{1}{\delta t} \sum_{t=t_0}^{t_0+\delta t} \frac{\partial N^2}{\partial t}\bigg|_t \tag{6}$$

$$\Delta N^2_{model} = N^2_{t_0+\delta t} - N^2_{t_0} \tag{7}$$

$$Residual = \Delta N^2_{model} - \Delta N^2_{budget} \tag{8}$$

where t_0 is an initial time and δt is 24 hours.

Eqs. 6-8 are plotted for three consecutive 24-hour periods in Fig. A2. For this and all subsequent radial-vertical cross sections, a 1-2-1 smoother is applied once in the radial direction to eliminate $2\Delta r$ noise that appears in some of the raw model output and calculated fields. The left column of Fig. A2 depicts the model changes (Eq. 7), the center column depicts the budget changes (Eq. 6), and the right column depicts the residuals (Eq. 8). In every 24-hour period, the budget changes are nearly identical to the model changes, which is reflected in the near-zero residuals in the right column. This indicates that the budget accurately represents the model variability, which implies that the neglect of moisture in the budget computation introduces negligible error within the anaysis domain[3].

---

[2]These terms include the tendencies due to implicit diffusion in the fifth-order finite differencing scheme.

[3]This is not the case in the lower- and mid-troposphere, where the residual actually exceeds the budget variability in many places, likely due to the neglect of moisture; thus we limit this analysis to the upper troposphere and lower stratosphere.

In the tropopause layer, some of the budget terms are small enough to be ignored. To determine which of the budget terms are most important, a time series of the contribution of each of the budget terms in Eq. 5 to the tropopause-layer static stability tendency is plotted in Fig. A4. For this figure, each of the budget terms is computed using the method described in Section 3, except with 1-hour averaging intervals instead of 24-hour intervals. The absolute values of these tendencies are then averaged over a radius-height domain surrounding the tropopause and plotted as a time series[4]. Advection (Fig. A4, red line) plays an important role in the mean tropopause-layer static stability tendency at all times, and vertical turbulence (Fig. A4, blue line) and radiation (Fig. A4, dark green line) also contribute significantly. Although the contribution from horizontal turbulence (Fig. A4, purple line) becomes more important after 48 hours, it is confined to a very small region immediately surrounding the eyewall tangential velocity maximum (not shown), and is negligible throughout the rest of the tropopause layer. The two remaining processes - microphysics and dissipative heating (Fig. A4, orange and light green lines, respectively) - lie atop one another near zero. Although the latent heating term can be quite large in the eyewall region, it is negligible everywhere outside of the eyewall, as are the effects of dissipative heating.

The preceding analysis indicates that, at all times, three budget terms dominate the tropopause-layer static stability tendency: advection, vertical turbulence, and radiation. Variations in the magnitude and spatial structure of these terms drive the static stability changes depicted in Fig. A2; subsequent sections will focus on these variations and what causes them.

---

[4]It will be seeen in subsequent figures that each of the terms contributes both positively and negatively to the N^2 tendency within the analysis domain. Thus, taking an average over the domain tends to wash out the positive and negative contributions. To circumvent this problem, the absolute value of each of the terms is averaged.

4. Results

a. Static stability evolution

The average N^2 over the first day of the simulation (Fig. A3a) indicates the presence of a weak static stability maximum just above the cold-point tropopause. Over the subsequent 24 hours, during the RI period, the static stability within and above this layer decreased near the storm center (Fig. A3b). This decreasing N^2 corresponded to an increase in the tropopause height within the developing eye, maximized at the storm center. Outside of the eye, meanwhile, the tropopause height decresed over the eyewall region (25-60-km radius) and increased only slightly outside of the 60-km radius. In this outer region, the N^2 maximum just above the tropopause strengthened during RI. These trends continued as the storm's intensity leveled off in the 48-72-hour period (Fig. A3c). The tropopause height increased to nearly 21 km at the storm center and sloped sharply downward to 16.3 km on the inner edge of the eyewall, near the 30 km radius. Static stability outside of the eye, meanwhile, continued to increase just above the cold-point tropopause. This N^2 evolution closely follows that observed in Hurricane Patricia (2015; Duran and Molinari 2018). The mechanisms that led to these static stability changes will be investigated in the subsequent sections.

b. Static stability budget analysis

(i) 0-24 hours The weakening of the lower-stratospheric static stability maximum during the initial spin-up period is reflected in the total N^2 budget change over this time (Fig. A5a). The 17-18-km layer was characterized by decreasing N^2 (purple shading), maximizing at the storm center. The layer immediately below the tropopause, meanwhile, saw strengthening N^2 during this time period. Although these tendencies extended out to the 200-km radius, they were particularly

pronounced at innermost radii. A comparison of the contributions of advection (Fig. A5b), vertical turbulence (Fig. A5c), and radiation (Fig. A5d) reveals that advection was primarily responsible for the change in static stability during this period. Although vertical turbulence acted in opposition to advection (i.e. it acted to stabilize regions that advection acted to destabilize), the magnitude of the advective tendencies was larger, particularly at the innermost radii. The sum of advection and vertical turbulence (Fig. A5e) almost exactly replicated the static stability tendencies above 17 km. Radiative tendencies, meanwhile, (Fig. A5d) acted to destabilize the layer below about 16 km and stabilize the layer between 16 and 17 km. The sum of advection, vertical turbulence, and radiation (Fig. A5f) reproduces the total change in N^2 almost exactly.

(ii) 24-48 hours During the RI period, N^2 within the eye generally decreased above 16 km and increased below (Fig. A6a). These tendencies at the innermost radii were driven almost entirely by advection (Fig. A6b); vertical turbulence (Fig. A6c) and radiation (Fig. A6d) contributed negligibly to the static stability tendencies in this region.

Outside of the eye, the N^2 evolution exhibited alternating layers of positive and negative tendencies. Near and above 18 km existed an upward-sloping region of decreasing N^2 that extended out to the 180-km radius. In this region, neither vertical turbulence nor radiation exhibited negative N^2 tendencies; advection was the only forcing for destabilization. Immediately below this layer was a region of increasing N^2, which sloped upward from 17 km near the 30-km radius to just below 18 km outside of the 100-km radius. Advection and vertical turbulence both contributed to this positive N^2 tendency, with advection playing an important role below about 17.5 km and and turbulence playing an important role above. The sum of advection and turbulence (Fig. A6e) reveals two discontiguous regions of increasing N^2 in the 17-18-km layer rather than one contiguous region. The addition of radiation to these two terms, however, (Fig. A6f) provides the link between these two regions, indicating that radiation also plays a role in strengthening the stable layer just above the tropopause. In the 16-17-km layer, a horizontally-extensive layer of decreasing N^2 also was forced by a combination of advection, vertical turbulence, and radiation. The sum of advection and vertical turbulence accounts for only a portion of the decreasing N^2 in this layer, and actually indicates forcing for stabilization near the 50-km radius and outside of the 130-km radius. Radiative tendencies overcome this forcing for stabilization in both of these regions to produce the radially-extensive region of destabilization observed just below the tropopause.

The sum of advection, vertical turbulence, and radiation (Fig. A6f) once again closely follows the observed N^2 variability, except in portions of the eyewall where the neglect of latent heating and horizontal turbulence introduces some differences.

(iii) 48-72 hours After the storm's maximum wind speed leveled off near 80 m s^{-1}, the magnitude of the static stability tendencies within the eye decreased to near zero (Fig. A7a).

Outside of the eye, however, N^2 continued to increase just above the tropopause and decrease just below. The sum of advection and vertical turbulence (Fig. A7e) indicates that the increase of N^2 observed in the 17-18-km layer and inside of the 80-km radius cannot be attributed to these processes, since the sum of these two terms provided forcing for destabilization. Instead, radiation (Fig. A7d), provided the forcing for stabilization in this region. Outside of the 80-km radius, both advection (Fig. A7b) and vertical turbulence (Fig. A7c) provided forcing for stabilization near the 18-km level. The sum of the two terms indicates increasing N^2 near the 18-km level everywhere outside of the 80-km radius, but this stabilization is slightly weaker in the 90-120-km radial band than the observed value. The addition of radiation (Fig. A7f) provides the extra forcing for stabilization required to account for the observed increase in N^2. Outside of the 120-km radius, the region of radiative forcing for stabilization slopes downward, and the increase in N^2 observed near

18 km can be explained entirely by a combination of advection and vertical turbulence. The layer of decreasing N^2 observed near 17 km was forced primarily by vertical turbulence and radiation. Within most of this region, advection provided strong forcing for stabilization, but this forcing was outweighed by the negative N^2 tendencies induced by a combination of vertical turbulence and radiation.

5. Discussion

a. The role of advection

Advection played an important role in the tropopause-layer N^2 evolution at all stages of intensification, but for brevity, this section will focus only on the RI (24-48-hour) period. To investigate the advective processes more closely, the individual contributions of horizontal and vertical advection during the RI period are shown in Fig. A8, along with the corresponding time-mean radial and vertical velocities and θ. The N^2 tendencies due to the two advective components (Fig. A8a,b) exhibit strong cancellation, consistent with flow that is nearly isentropic. There are, however, many regions in which flow crosses θ surfaces; this flow accounts for all non-zero N^2 tendencies due to advection previously seen in Fig. A6b.

During the RI period, strong radial and vertical circulations developed near the tropopause, which forced high-magnitude N^2 tendencies due to advection (Fig. A8a,b). A layer of strong outflow developed at and below the tropopause during this period, with the outflow maximum (dashed cyan line) curving from the 14-km level at the 50-km radius to just below the 16-km level outside of the 80-km radius (Fig. A8c). Notably, the N^2 tendency due to horizontal advection (Fig. A8a) tended to switch signs at this line, with stabilization below the outflow maximum and destabilization above. Outside of the eye and eyewall, isentropes generally sloped upward with radius. Vertical wind shear acting on these upward-sloping isentropes should act to tilt them into the vertical above the outflow maximum, thereby decreasing $\partial\theta/\partial z$, and tilt them to be more horizontal below the outflow maximum, thereby increasing $\partial\theta/\partial z$. This mechanism is the same as that discussed in Trier and Sharman (2009), and is consistent with the change in sign of the N^2 tendency at the level of maximum outflow.

Meanwhile in the lower stratosphere, a thin layer of 2-4 m s^{-1} inflow developed a few hundred meters above the tropopause, similar to that which was observed in Hurricane Patricia (2015; Duran and Molinari 2018) and in previous modeling studies (e.g. Ohno and Satoh 2015; Kieu et al. 2016). Since the isentropes in this layer sloped slightly upward with radius (i.e. $\partial\theta/\partial r < 0$), this inflow acted to import lower θ air from outer radii to inner radii. Since the negative θ tendencies maximized at the level of maximum inflow, the layer layer below the inflow maximum destabilized and the layer above stabilized (Fig. A8a).

Curiously, horizontal advection contributed to the N^2 tendency everywhere within the eye, even though the mean radial velocity was near zero. Close examination of the model output revealed that these tendencies were forced by advective processes associated with inward-propagating waves. Although the radial velocity perturbations induced by these waves averaged out to zero, the advective tendencies forced by the radial velocity perturbations did not. Additionally, when these waves reached r=0, a dipole of vertical velocity resulted, with ascent above and subsidence below. For reasons that remain unclear, the regions of ascent were more persistent than the regions of subsidence, which resulted in the mean ascent observed near r=0 above 17 km in Fig. A8b.

Vertical advection also played an important role in the tropopause-layer static stability evolution. Within the eye, subsidence dominated below 17 km, while mean ascent existed near the storm center above 17 km. Although the magnitude of the subsidence was larger at lower altitudes, $\partial\theta/\partial z$ was smaller there. Because $\partial\theta/\partial z$ was smaller, the subsidence at lower levels could not accomplish as much warming as the subsidence at higher levels in the eye, consistent with the results of Stern and Zhang (2013). As a result, vertical advection within the eye acted to stabilize the layer below 16 km during RI.

Outside of the eye, ascent dominated the troposphere, while a 1.5-km-deep layer of descent existed immediately above the tropopause. These regions of ascent and descent converged just above the tropopause; this convergence acted to compact the isentropes in this layer and increase the static stability. Above the lower-stratospheric subsidence maximum, meanwhile, vertical advection acted to decrease N^2. In the troposphere, vertical advection acted to increase N^2 within the eyewall region and above the vertical velocity maximum at larger radii. Outside of the eyewall and below the vertical velocity maximum, meanwhile, vertical advection acted to decrease N^2.

Comparing the N^2 tendencies due to horizontal (Fig. A8a) and vertical (Fig. A8b) advection to the total advective tendency seen in Fig. A6b reveals that horizontal advective tendencies dominated the troposphere, while vertical advective tendencies dominated the layer near and above the tropopause. Thus, tilting of isentropes in the vicinity of the upper-tropospheric outflow maximum appears to be the most important process governing the N^2 tendency in the troposphere, whereas convergence of vertical velocity appears to be the most important process near the tropopause.

b. The role of radiation

During the initial spin-up period (0-24 hours; A9a), convection was not deep enough to deposit large quantities of ice near the tropopause in the mean. Due to the lack of ice particles, the radiative heating tendencies during this period (Fig. A9b) were relatively small and confined to the region above a few particularly strong convective towers. During RI (24-48 hours; Fig. A9b), the eyewall updraft strengthened and a radially-extensive cirrus canopy developed near the tropopause. The enhanced vertical gradient of ice mixing ratio at the top of the cirrus canopy induced strong diurnal-mean radiative cooling near the tropopause (Fig. A9d). This cooling exceeded 0.6 K h^{-1} in some places and sloped downward from the lower stratosphere into the upper troposphere, following the top of the cirrus canopy. A small radiative warming maximum also appeared outside of the 140-km radius below this region of cooling. These results broadly agree with those of Bu et al. (2014; see their Fig. 11a), whose CM1 simulations produced a 0.3 K diurnally-averaged radiative cooling at the top of the cirrus canopy and radiative warming within the cloud that maximized near the 200-km radius. The broad region of radiative cooling acted to destabilize the layer below the cooling maximum and stabilize the layer above, which can be seen in Fig. A6d. The small area of net radiative heating outside of the 140-km radius enhanced the destabilization above 16 km in this region and produced a thin layer of stabilization in the 15-16-km layer.

After the TC's RI period completed (48-72 hours; Fig. A9f), strong radiative cooling remained near the tropopause at inner radii, sloping downward with the top of the cirrus canopy to below the tropopause at outer radii. Cooling rates exceeded 1 K h^{-1} just above the tropopause between the 30- and 70-km radii. These cooling rates exceeded those observed by Bu et al. (2014), a discrepancy that is a consequence of their larger vertical grid spacing (625 m) compared to that used here (250 m), along with a contribution from differing radiation schemes[5]. Time-mean radiative warming spread from 30- to 160-km radius within the cirrus canopy. The existence of radiative cooling overlying radiative warming in this region led to radiatively-forced destabilization at and below the tropopause, as was observed in Fig. A7d. Below the warming layer existed a region of forcing for stabilization, while a much stronger region of forcing for stabilization existed in the lower stratosphere, above the cooling maximum.

---

[5]Bu et al. (2014) employed the NASA-Goddard radiation scheme for their CM1 simulations, whereas RRTMG is used in the present paper. A simulation using NASA-Goddard radiation and 625-m vertical grid spacing produced maximum radiative cooling rates of 0.3 K h^{-1}, which agrees with the rates in Bu et al. (2014). Another simulation using 625-m vertical grid spacing and RRTMG radiation produced cooling rates of up to 0.6 K h^{-1}, which is consistent with the WRF simulations of Bu et al. (2014).

The results herein suggest that radiative heating tendencies played an important role in destabilizing the upper troposphere and stabilizing the lower stratosphere after the cirrus canopy developed.

c. The role of turbulent mixing

Although vertical turbulence always acts to eliminate vertical gradients of θ, this adjustment toward a neutral state only occurs where the mixing takes place. If turbulence occurs in a stably-stratified layer, it will act to decrease θ at the top of the layer and increase it below. Just above and just below the mixed layer, however, the θ profile remains undisturbed. Consequently, although turbulent mixing acts to decrease $\partial\theta/\partial z$ in the layer in which it is occurring, it actually increases $\partial\theta/\partial z$ just below and just above the layer. These vertical gradients of turbulent mixing are quite important, particularly on the flanks of the upper-tropospheric outflow jet.

Fig. A10 reveals that two distinct maxima of vertial eddy diffusivity developed in the tropopause layer as the storm intensified. Comparison of these turbulent regions to the N^2 tendencies in Figs. A6c and A7c reveals that the layers in which vertical eddy diffusivity maximized corresponded to layers of destabiliztion due to vertical turbulence. Just outside of these layers, however, vertical turbulence acted to increase N^2. The large vertical gradient of vertical eddy diffusivity near the tropopause played an important role in developing the lower-stratospheric stable layer during RI. This supports the hypothesized role of turbulence in setting the outflow-layer θ stratification in Rotunno and Emanuel (1987).

6. Conclusions

The simulated N^2 evolution shown herein closely matched that observed during the RI of Hurricane Patricia (2015). Three processes dominated the N^2 variability in the upper troposphere and lower stratosphere: advection, radiation, and vertical turbulence. Radiation and vertical turbulence played particularly important roles in developing the strong N^2 maximum just above the cold-point tropopause during RI. Since these two processes are parameterized, and radiation closely depends on yet another parameterized process (microphysics), the tropopause-layer N^2 variability could be quite sensitive to the assumptions inherent to the parameterizations used. A better understanding of the microphysical characteristics of the TC cirrus canopy, its interaction with radiation, and outflow-layer turbulence is critical to understanding the tropopause-layer N^2 evolution.

In this paper, all of the variables were averaged over a full diurnal cycle to eliminate the effects of diurnal variability and isolate the overall storm evolution. Diurnal variations in static stability near the tropopause are potentially of interest with respect to the tropical cyclone diurnal cycle, however, and will be the subject of future work.

Acknowledgments. We are indebted to George Bryan for his continued development and support of Cloud Model 1. We also thank Jeffrey Kepert, Robert Fovell, and Erika Navarro for helpful conversations related to this work. This research was supported by NSF Grant #1636799.

APPENDIX

Sensitivity experiments

The simulations exhibited some sentivity to the initial thermodynamic profile and the prescribed vertical mixing length. Although the details of the intensification and the tropopause-layer N^2 evolution varied when these quantities were changed, the conclusions of the paper remain unchanged.

a. Sensitivity to the initial thermodynamic profile

A number of sensitivity experiments were conducted using a variety of initial soundings. Changing the initial temperature and humidity profiles affected the timing of the onset of organized deep convection and the rapidity of intensification. In all simulations, however, convection eventually penetrated to the tropopause, at which time vertical turbulence and radiation combined with advection to adjust the N^2 profile toward that which was observed in the control run. By the end of the RI period in every simulation, all three proesses were actively modifying the N^2 profile near the tropopause.

As an example, 24-hour averages of N^2 are plotted in Fig. A1 for a simulation that was identical to that used in this paper, except the initial sounding was determined by averaging every grid point within 1000 km of TC Patricia's storm center at 18 UTC 21 October 2015 instead of averaging only within the 100-km radius. Although the lower-stratospheric stable layer developed more slowly and was weaker than that shown in Fig. A3, the overall evolution was quite similar and the same budget terms dominated the static stability evolution.

b. Sensitivity to the vertical mixing length

The rate of turbulent mixing in the Smagorinsky scheme used herein is highly dependent on a prescribed length scale. The vertical mixing length used in this paper (100 m) was based on the sensitivity experiments of Bryan (2012). Prescribing a smaller mixing length produces smaller θ tendencies due to turbulence, but even with a mixing length on the low end of those tested by Bryan (2012), turbulence still played an important role in the tropopause-layer N^2 evolution. Fig. A2 shows the 24-hour-averaged contributions of turbulent mixing to the N^2 evolution from a simulation identical to that used in this paper, except with a vertical mixing length of 50 m. At all times, vertical turbulence still played an important role in the tropopause-layer static stability evolution, particularly during the latter stages of RI (48-72 hours).

References

Bryan, G. H., 2012: Effects of surface exchange coefficients and turbulence length scales on the intensity and structure of numerically simulated hurricanes. *Mon. Wea. Rev.*, **140**, 1125–1143.

Bryan, G. H., and R. Rotunno, 2009: The maximum intensity of tropical cyclones in axisymmetric numerical model simulations. *Mon. Wea. Rev.*, **137**, 1770–1789.

Bu, Y. P., R. G. Fovell, and K. L. Corbosiero, 2014: Influence of cloud-radiative forcing on tropical cyclone structure. *J. Atmos. Sci.*, **71**, 1644–1622.

Doyle, J. D., and Coauthors, 2017: A view of tropical cyclones from above: The Tropical Cyclone Intensity (TCI) Experiment. *Bull. Amer. Meteor. Soc.*, **98**, 2113–2134.

Duran, P., and J. Molinari, 2018: Dramatic inner-core tropopause variability during the rapid intensification of Hurricane Patricia (2015). *Mon. Wea. Rev.*, **146**, 119–134.

Emanuel, K., 2012: Self-stratification of tropical cyclone outflow. Part II: Implications for storm intensification. *J. Atmos. Sci.*, **69**, 988–996.

Emanuel, K., and R. Rotunno, 2011: Self-stratification of tropical cyclone outflow. Part I: Implications for storm structure. *J. Atmos. Sci.*, **68**, 2236–2249.

Iacono, M. J., J. S. Delamere, E. J. Mlawer, M. W. Shephard, S. A. Clough, and W. D. Collins, 2008: Radiative forcing by long-lived greenhouse gases: Calculations with the AER radiative transfer models. *J. Geophys. Res.*, **113 (D13103)**.

Kepert, J. D., J. Schwendike, and H. Ramsay, 2016: Why is the tropical cyclone boundary layer not ”well mixed”? *J. Atmos. Sci.*, **73**, 957–973.

Kieu, C., V. Tallapragada, D.-L. Zhang, and Z. Moon, 2016: On the development of double warm-core structures in intense tropical cyclones. *J. Atmos. Sci.*, **73**, 4487–4506.

Kimberlain, T. B., E. S. Blake, and J. P. Cangialosi, 2016: Tropical cyclone report: Hurricane Patricia. National Hurricane Center. [Available online at www.nhc.noaa.gov].

Komaromi, W. A., and J. D. Doyle, 2017: Tropical cyclone outflow and warm core structure as revealed by HS3 dropsonde data. *Mon. Wea. Rev.*, **145**, 1339–1359.

Markowski, P. M., and G. H. Bryan, 2016: LES of laminar flow in the PBL: A potential problem for convective storm simulations. *Mon. Wea. Rev.*, **144**, 1841–1850.

Ohno, T., and M. Satoh, 2015: On the warm core of a tropical cyclone formed near the tropopause. *J. Atmos. Sci.*, **72**, 551–571.

Rogers, R. F., S. Aberson, M. M. Bell, D. J. Cecil, J. D. Doyle, J. Morgerman, L. K. Shay, and C. Velden, 2017: Re-writing the tropical record books: The extraordinary intensification of Hurricane Patricia (2015). *Bull. Amer. Meteor. Soc.*, **98**, 2091–2112.

Rotunno, R., and K. A. Emanuel, 1987: An air-sea interaction theory for tropical cyclones. Part II: Evolutionary study using a nonhydrostatic axisymmetric numerical model. *J. Atmos. Sci.*, **44**, 542–561.

Stern, D. P., and F. Zhang, 2013: How does the eye warm? Part I: A potential temperature budget analysis of an idealized tropical cyclone. *J. Atmos. Sci.*, **70**, 73–89.

Thompson, G., R. M. Rasmussen, and K. Manning, 2004: Explicit forecasts of winter precipitation using an improved bulk microphysics scheme. Part I: Description and sensitivity analysis. *Mon. Wea. Rev.*, **132**, 519–542.

Trier, S. B., and R. D. Sharman, 2009: Convection-permitting simulations of the environment supporting widespread turbulence within the upper-level outflow of a mesoscale convective system. *Mon. Wea. Rev.*, **137**, 1972–1990.

LIST OF FIGURES

Fig. 1. The maximum 10-m wind speed (top panel; m s^{-1}) and minimum sea-level pressure (bottom panel; hPa) in the simulated storm (blue lines) and from Hurricane Patricia's best track (red stars). 24

Fig. 2. Left panels: Twenty-four-hour changes in squared Brunt-Väisälä frequency (N^2; 10^{-4} s^{-2}) over (top row) 0-24 hours, (middle row) 24-48 hours, (bottom row) 48-72 hours. Middle Panels: The N^2 change over the same time periods computed using Eqs. 4-6, Right Panels: The budget residual over the same time periods, computed by subtracting the budget change (middle column) from the model change (left column). 25

Fig. 3. Twenty-four-hour averages of squared Brunt-Väisälä frequency (N^2; 10^{-4} s^{-2}) over (a) 0-24 hours, (b) 24-48 hours, (c) 48-72 hours. Orange lines represent the cold-point tropopause averaged over the same time periods. 26

Fig. 4. Time series of the contribution of each of the budget terms to the time tendency of the squared Brunt-Väisälä frequency (N^2; 10^{-4} s^{-2}). For each budget term, the absolute value of the N^2 tendency is averaged temporally over 1-hour periods (using output every minute), and spatially in a region extending from 0 to 200 km radius and 14 to 21 km altitude. 27

Fig. 5. (a) Total change in N^2 over the 0-24-hour period (10^{-4} s^{-2} $(24\ h)^{-1}$) and the contributions to that change from (b) the sum of horizontal and vertical advection, (c) vertical turbulence, (d) longwave and shortwave radiation, (e) the sum of horizontal advection, vertical advection, and vertical turublence, and (f) the sum of horizontal advection, vertical advection, vertical turbulence, and longwave and shortwave radiation. 29

Fig. 6. As in Fig. 5, but for the 24-48-hour period. 30

Fig. 7. As in Fig. 5, but for the 48-72-hour period. 31

Fig. 8. The contribution to the change in N^2 over the 24-48-hour period (10^{-4} s^{-2} $(24\ h)^{-1}$) by (a) horizontal advection and (b) vertical advection. (c) The radial velocity (m s^{-1}; filled contours), potential temperature (K; thick black contours), cold-point tropopause height (orange line), and level of maximum outflow (dashed cyan line) averaged over the 24-48-hour period. (d) The vertical velocity (cm s^{-1}; filled contours), potential temperature (K; thick black contours), and cold-point tropopause height (orange line) averaged over the 24-48-hour period. 32

Fig. 9. Ice mixing ratio (g kg^{-1}) and cold-point tropopause height (orange lines) averaged over (a) 0-24 hours, (c) 24-48 hours, and (e) 48-72 hours. Radiative heating rate (K h^{-1}) and cold-point tropopause height (orange lines) averaged over (b) 0-24 hours, (d) 24-48 hours, and (f) 48-72 hours. 34

Fig. 10. Vertical eddy diffusivity (m^2 s^{-2}; filled contours), cold-point tropopause height (cyan lines), and radial velocity (m s^{-1}; thick black lines) averaged over (a) 0-24 hours, (b) 24-48 hours, and (c) 48-72 hours. 35

Fig. A1. Twenty-four-hour averages of squared Brunt-Väisälä frequency (N^2; 10^{-4} s^{-2}) over (a) 0-24 hours, (b) 24-48 hours, (c) 48-72 hours, and (d) 72-96 hours for the simulation described in Appendix Aa. Orange lines represent the cold-point tropopause averged over the same time periods. 36

Fig. A2. The contribution of vertical turbulence to the N^2 variability (10^{-4} s^{-2} $(24\ h)^{-1}$) averaged over (a) 0-24 hours, (b) 24-48 hours, (c) 48-72 hours, and (d) 72-96 hours for the simulation described in Appendix Ab. 37

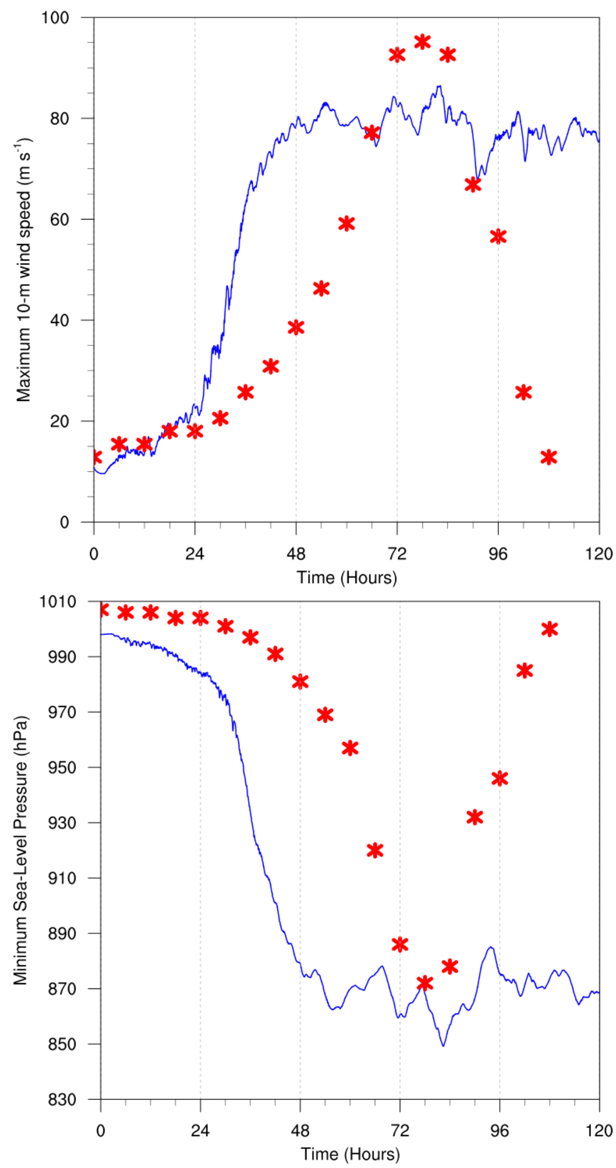

461 FIG. 1. The maximum 10-m wind speed (top panel; m s^{-1}) and minimum sea-level pressure (bottom panel; 462 hPa) in the simulated storm (blue lines) and from Hurricane Patricia's best track (red stars).

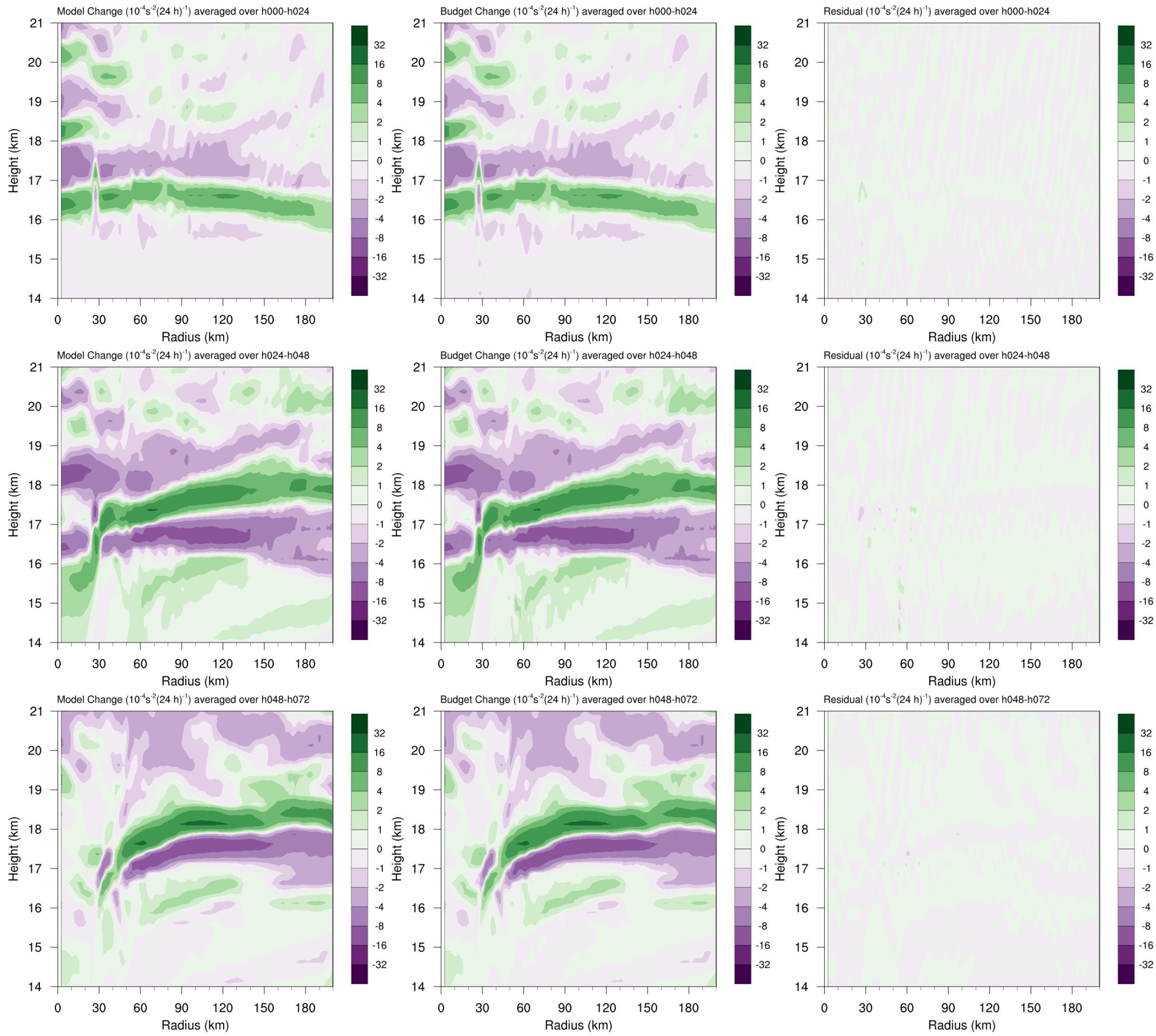

FIG. 2. Left panels: Twenty-four-hour changes in squared Brunt-Väisälä frequency (N^2; 10^{-4} s^{-2}) over (top row) 0-24 hours, (middle row) 24-48 hours, (bottom row) 48-72 hours. Middle Panels: The N^2 change over the same time periods computed using Eqs. 4-6, Right Panels: The budget residual over the same time periods, computed by subtracting the budget change (middle column) from the model change (left column).

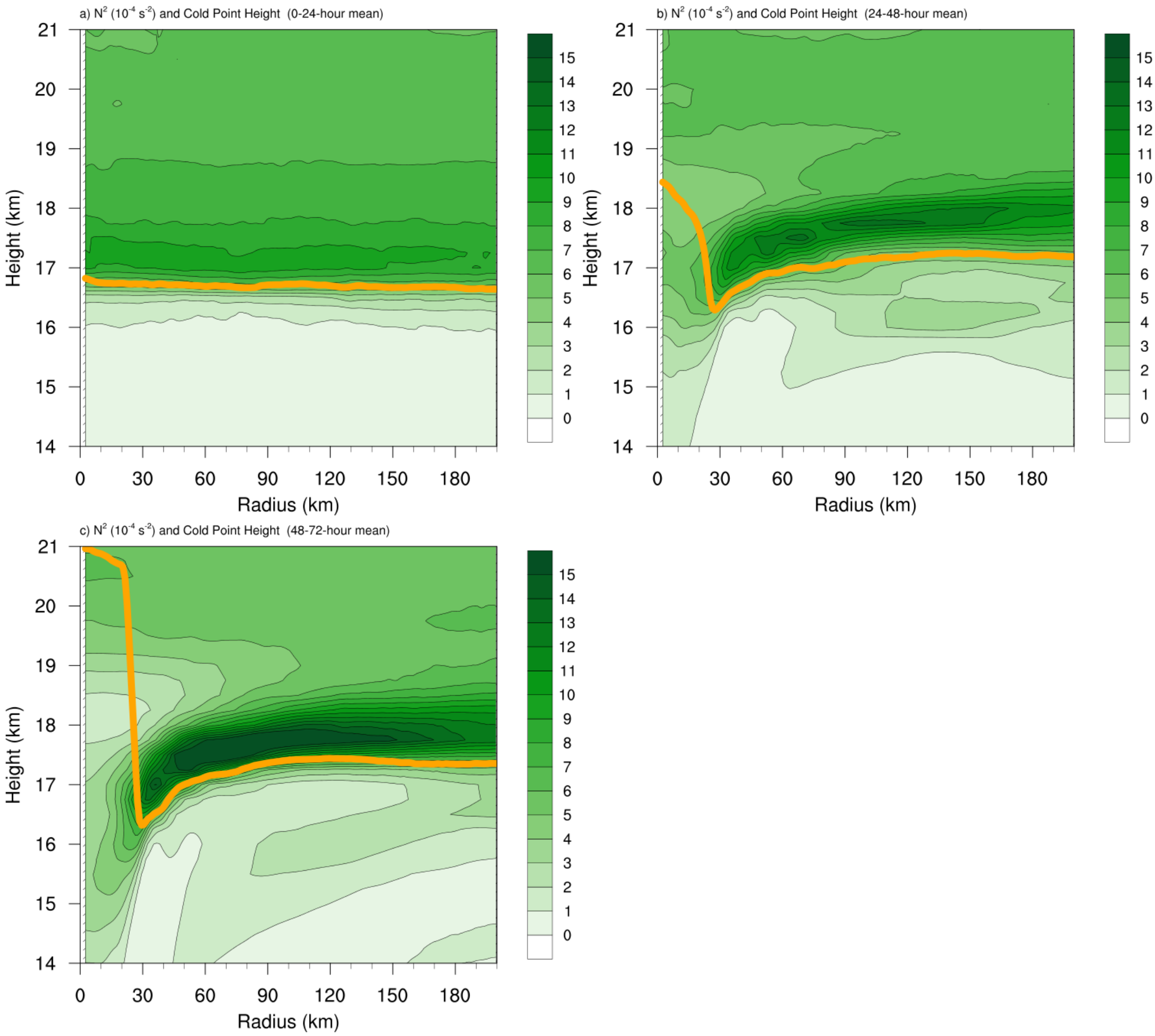

FIG. 3. Twenty-four-hour averages of squared Brunt-Väisälä frequency (N^2; 10^{-4} s^{-2}) over (a) 0-24 hours, (b) 24-48 hours, (c) 48-72 hours. Orange lines represent the cold-point tropopause averaged over the same time periods.

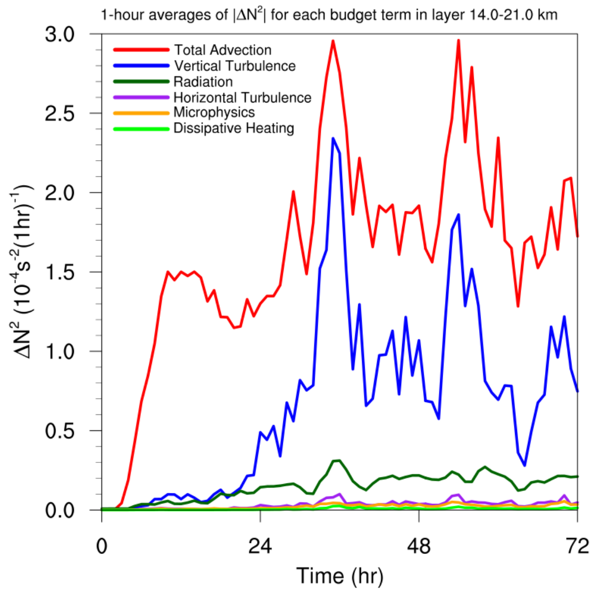

FIG. 4. Time series of the contribution of each of the budget terms to the time tendency of the squared Brunt-Väisälä frequency (N^2; 10^{-4} s^{-2}). For each budget term, the absolute value of the N^2 tendency is averaged temporally over 1-hour periods (using output every minute), and spatially in a region extending from 0 to 200 km radius and 14 to 21 km altitude.

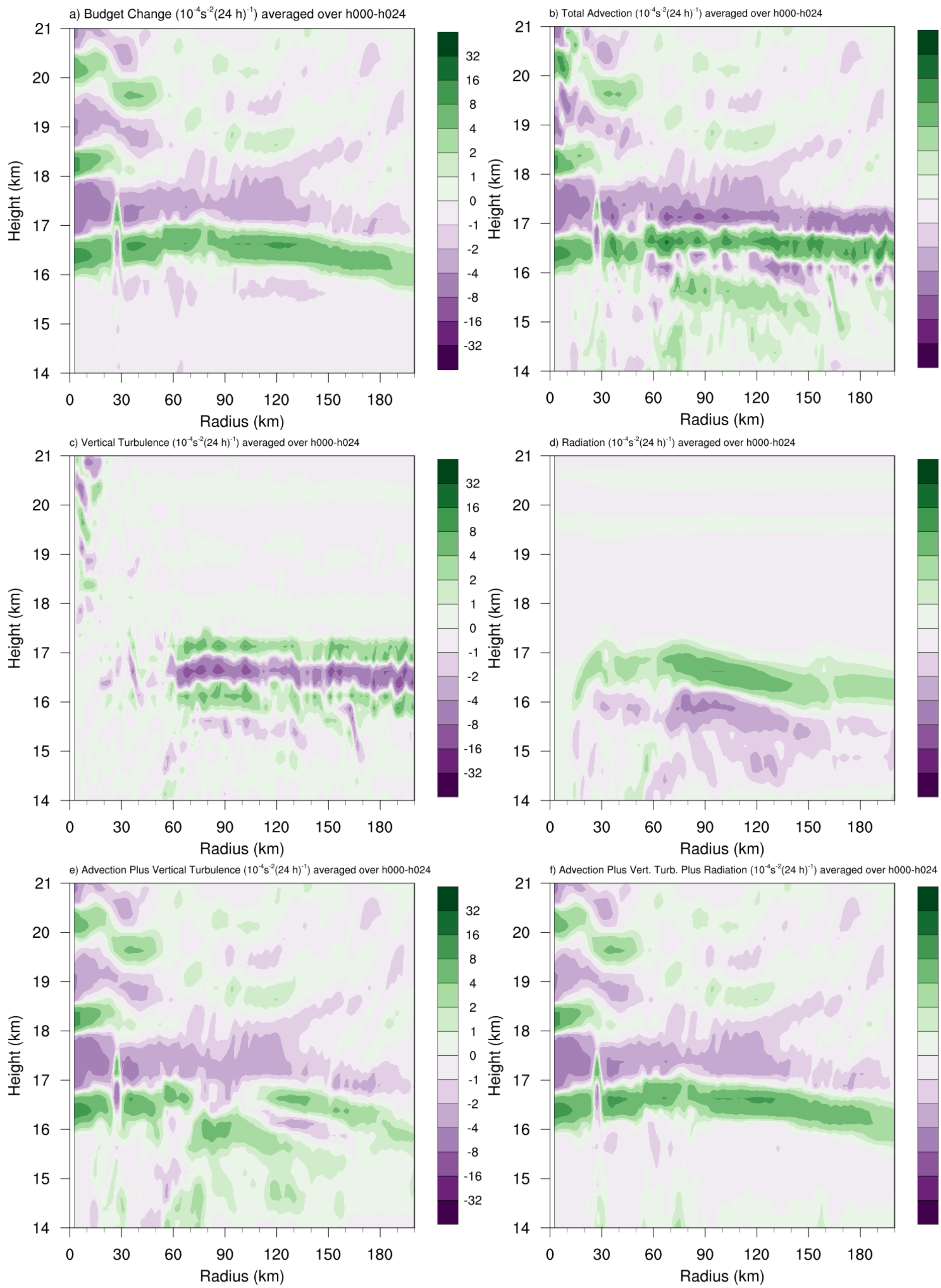

a) Budget Change ($10^{-4}s^{-2}(24\ h)^{-1}$) averaged over h000-h024
b) Total Advection ($10^{-4}s^{-2}(24\ h)^{-1}$) averaged over h000-h024
c) Vertical Turbulence ($10^{-4}s^{-2}(24\ h)^{-1}$) averaged over h000-h024
d) Radiation ($10^{-4}s^{-2}(24\ h)^{-1}$) averaged over h000-h024
e) Advection Plus Vertical Turbulence ($10^{-4}s^{-2}(24\ h)^{-1}$) averaged over h000-h024
f) Advection Plus Vert. Turb. Plus Radiation ($10^{-4}s^{-2}(24\ h)^{-1}$) averaged over h000-h024
Height (km)
Radius (km)

FIG. 5. (a) Total change in N^2 over the 0-24-hour period (10^{-4} s^{-2} $(24\ h)^{-1}$) and the contributions to that change from (b) the sum of horizontal and vertical advection, (c) vertical turbulence, (d) longwave and shortwave radiation, (e) the sum of horizontal advection, vertical advection, and vertical turublence, and (f) the sum of horizontal advection, vertical advection, vertical turbulence, and longwave and shortwave radiation.

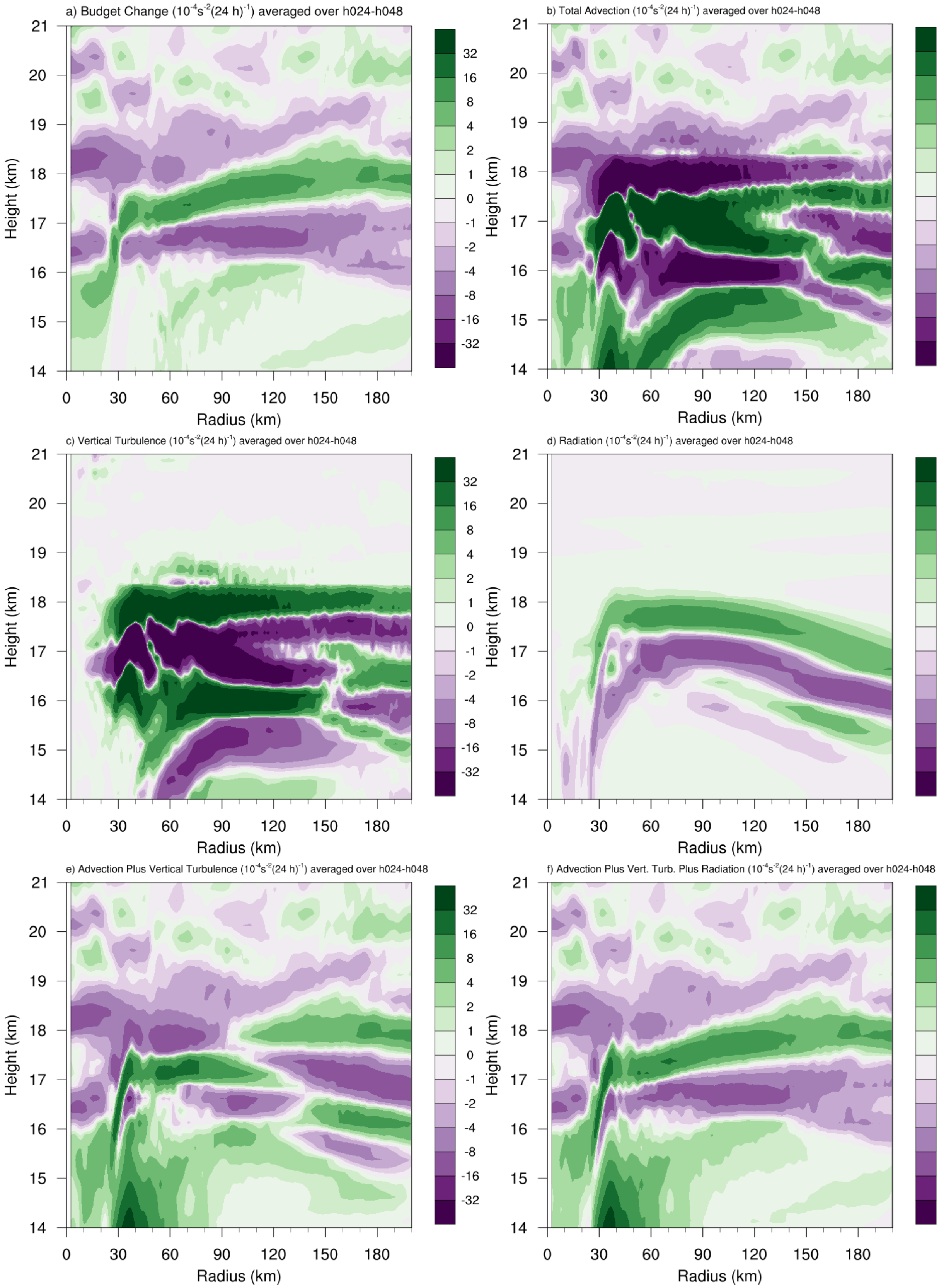

FIG. 6. As in Fig. A5, but for the 24-48-hour period.

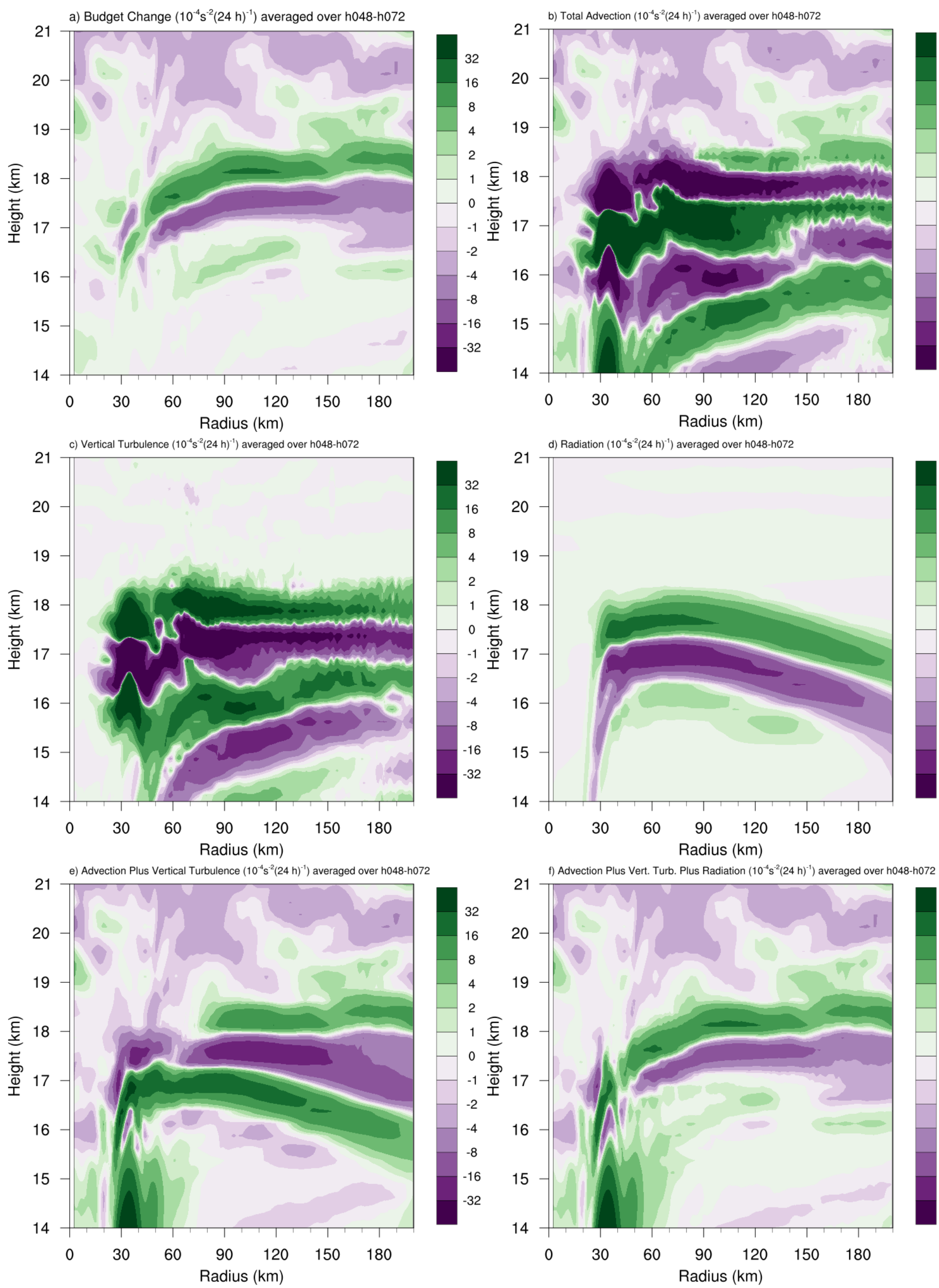

FIG. 7. As in Fig. A5, but for the 48-72-hour period.

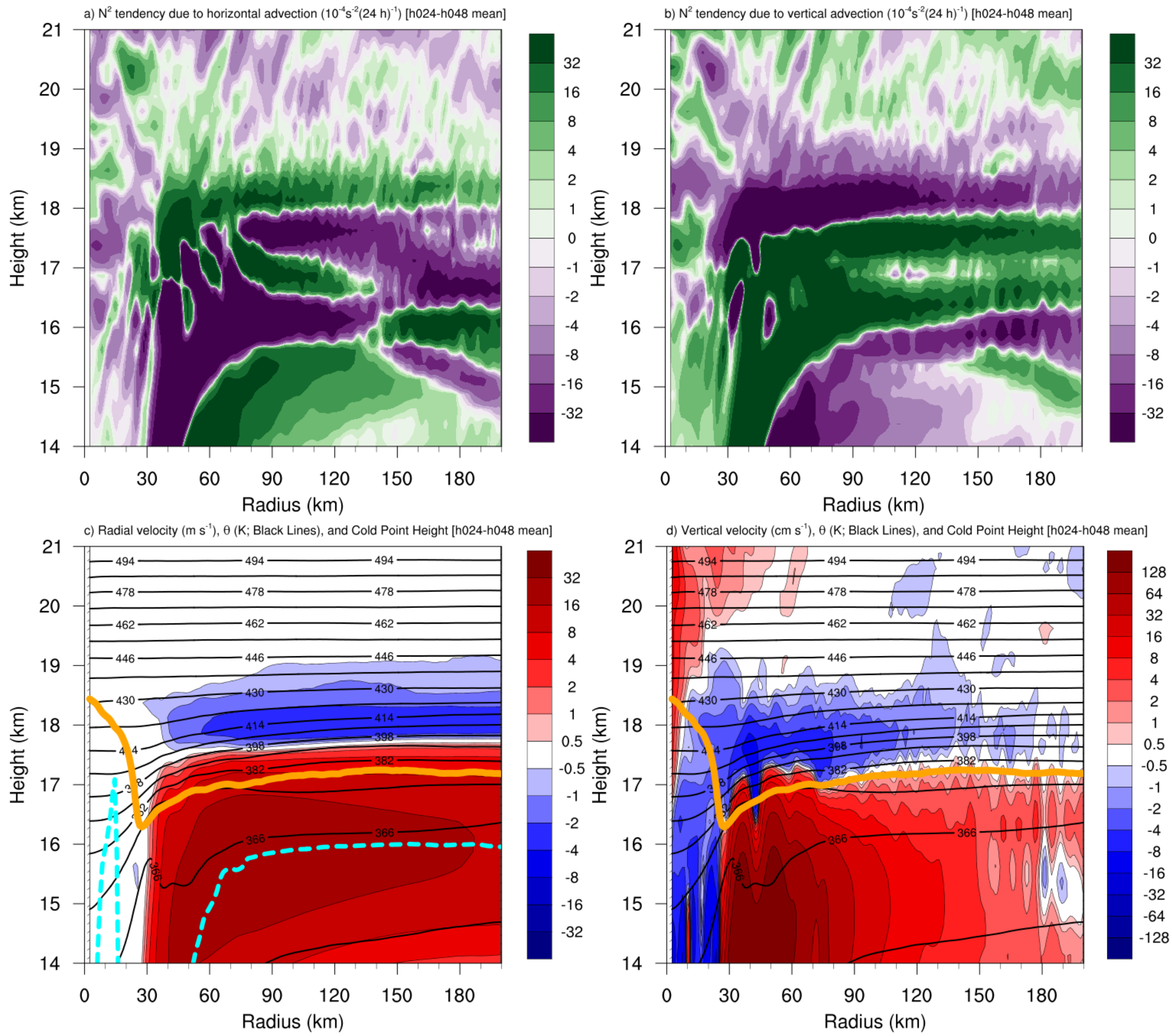

FIG. 8. The contribution to the change in N^2 over the 24-48-hour period (10^{-4} s^{-2} (24 h)$^{-1}$) by (a) horizontal advection and (b) vertical advection. (c) The radial velocity (m s^{-1}; filled contours), potential temperature (K; thick black contours), cold-point tropopause height (orange line), and level of maximum outflow (dashed cyan line) averaged over the 24-48-hour period. (d) The vertical velocity (cm s^{-1}; filled contours), potential temperature (K; thick black contours), and cold-point tropopause height (orange line) averaged over the 24-48-hour period.

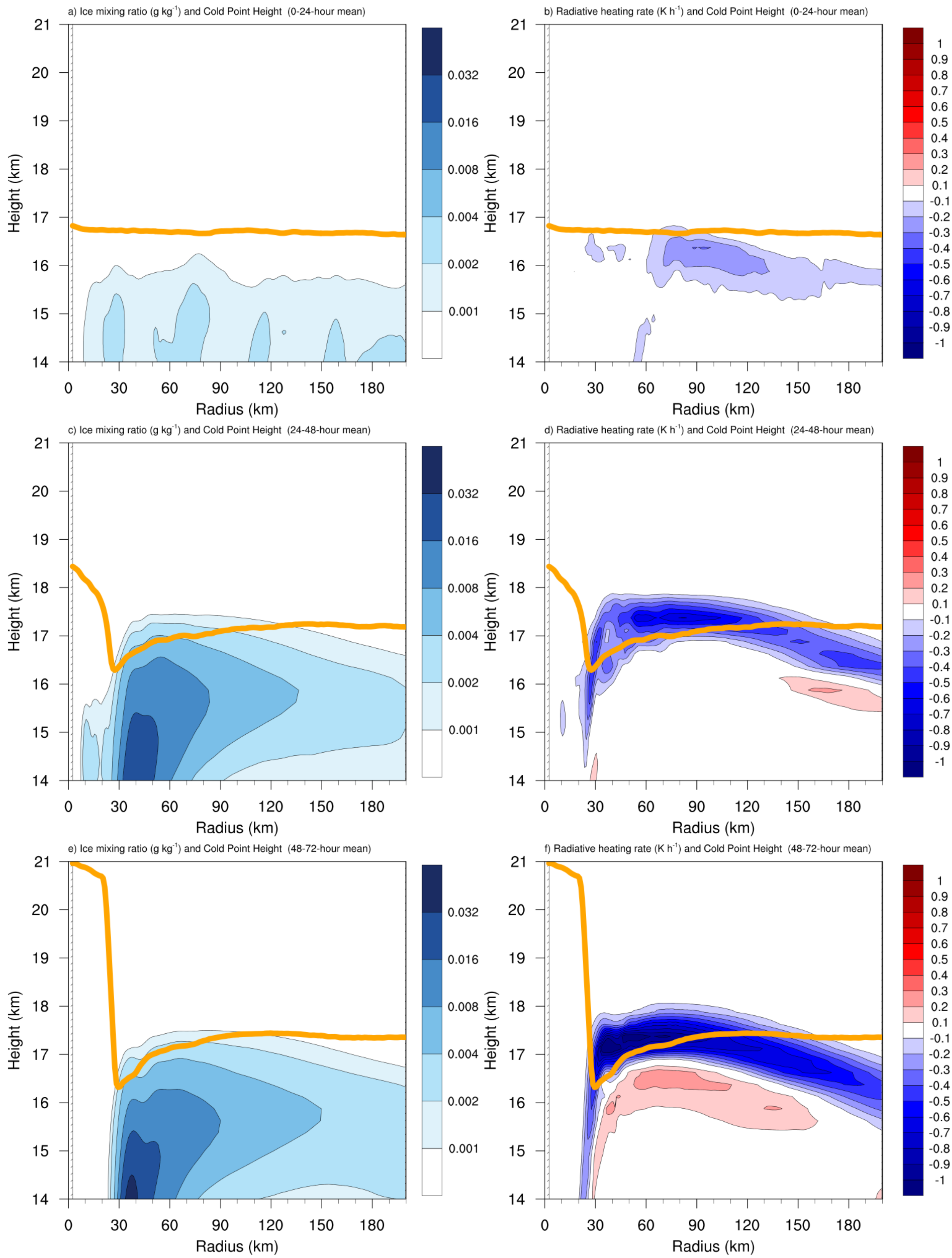

a) Ice mixing ratio (g kg-1) and Cold Point Height (0-24-hour mean)
b) Radiative heating rate (K h-1) and Cold Point Height (0-24-hour mean)
c) Ice mixing ratio (g kg-1) and Cold Point Height (24-48-hour mean)
d) Radiative heating rate (K h-1) and Cold Point Height (24-48-hour mean)
e) Ice mixing ratio (g kg-1) and Cold Point Height (48-72-hour mean)
f) Radiative heating rate (K h-1) and Cold Point Height (48-72-hour mean)
Height (km)
Radius (km)

FIG. 9. Ice mixing ratio (g kg^{-1}) and cold-point tropopause height (orange lines) averaged over (a) 0-24 hours, (c) 24-48 hours, and (e) 48-72 hours. Radiative heating rate (K h^{-1}) and cold-point tropopause height (orange lines) averaged over (b) 0-24 hours, (d) 24-48 hours, and (f) 48-72 hours.

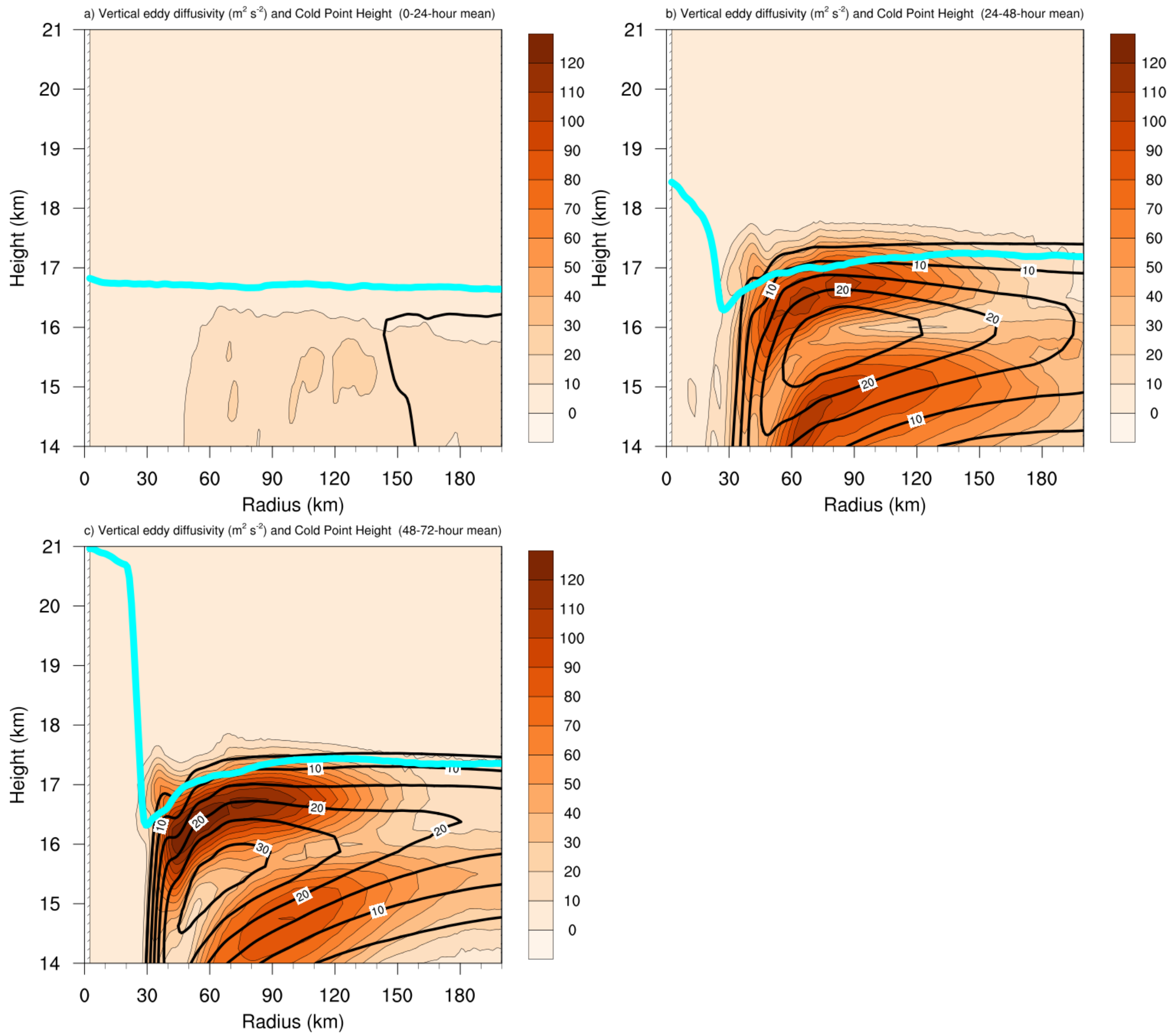

487 FIG. 10. Vertical eddy diffusivity (m^2 s^{-2}; filled contours), cold-point tropopause height (cyan lines), and radial velocity (m s^{-1}; thick black lines) averaged over (a) 0-24 hours, (b) 24-48 hours, and (c) 48-72 hours.

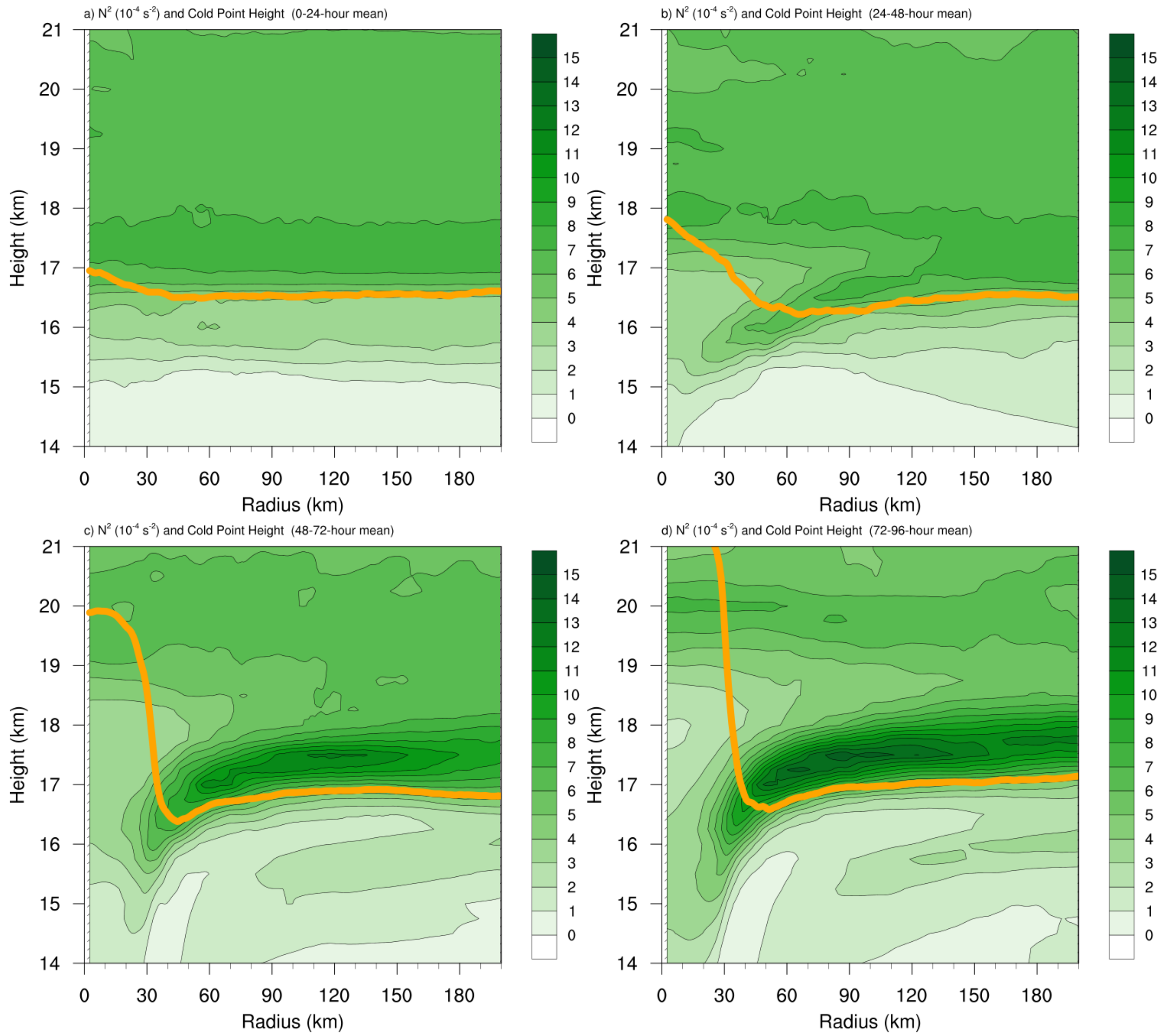

Fig. A1. Twenty-four-hour averages of squared Brunt-Väisälä frequency (N^2; 10^{-4} s^{-2}) over (a) 0-24 hours, (b) 24-48 hours, (c) 48-72 hours, and (d) 72-96 hours for the simulation described in Appendix Aa. Orange lines represent the cold-point tropopause averged over the same time periods.

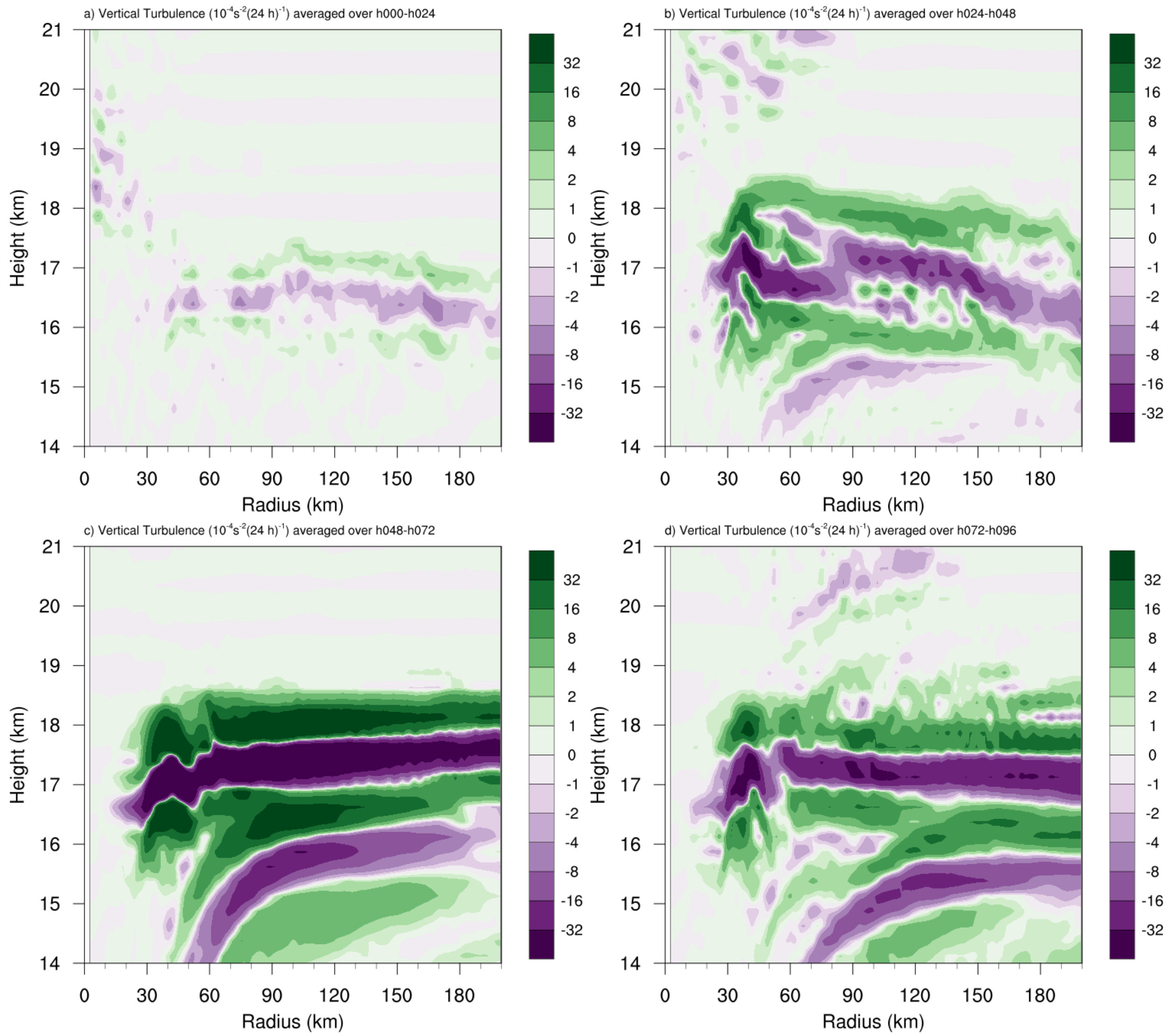

Fig. A2. The contribution of vertical turbulence to the N^2 variability (10^{-4} s^{-2} (24 h)$^{-1}$) averaged over (a) 0-24 hours, (b) 24-48 hours, (c) 48-72 hours, and (d) 72-96 hours for the simulation described in Appendix Ab.